ARTICLE

Check for updates

Sideband-resolved resonator electromechanics based on a nonlinear Josephson inductance probed on the single-photon level

Philip Schmidt [1,2], Mohammad T. Amawi[1,2], Stefan Pogorzalek[1,2], Frank Deppe [1,2,3], Achim Marx[1], Rudolf Gross[1,2,3] & Hans Huebl [1,2,3 ✉]

Light-matter interaction in optomechanical systems is the foundation for ultra-sensitive detection schemes as well as the generation of phononic and photonic quantum states. Electromechanical systems realize this optomechanical interaction in the microwave regime. In this context, capacitive coupling arrangements demonstrated interaction rates of up to 280 Hz. Complementary, early proposals and experiments suggest that inductive coupling schemes are tunable and have the potential to reach the single-photon strong-coupling regime. Here, we follow the latter approach by integrating a partly suspended super-conducting quantum interference device (SQUID) into a microwave resonator. The mechanical displacement translates into a time varying flux in the SQUID loop, thereby providing an inductive electromechanical coupling. We demonstrate a sideband-resolved electromechanical system with a tunable vacuum coupling rate of up to 1.62 kHz, realizing sub-aN Hz$^{-1/2}$ force sensitivities. The presented inductive coupling scheme shows the high potential of SQUID-based electromechanics for targeting the full wealth of the intrinsically nonlinear optomechanics Hamiltonian.

[1] Walther-Meißner-Institut, Bayerische Akademie der Wissenschaften, Walther-Meißner-Str. 8, 85748 Garching, Germany. [2] Physik-Departement, Technische Universität München, James-Franck-Str. 1, 85748 Garching, Germany. [3] Munich Center for Quantum Science and Technology (MCQST), Schellingstr. 4, D-80799 München, Germany. ✉email: huebl@wmi.badw.de

D esigning, investigating, and understanding the opto-
mechanical interaction plays a key role in tailoring the
light-matter interaction and hence for testing quantum
mechanics[1–4]. In addition, optomechanics is also the basis for
detection schemes with extreme sensitivity used in gravitational
wave detection[5], mechanical sensing[6] as well as the creation of
mechanical quantum states[7,8]. This potential triggered a multitude
of realizations of optomechanical systems[4,9] including systems
based on superconducting circuits, which define the field of nano-
electromechanics[10–16]. Here, the photonic cavity is implemented
as a microwave resonator and the electromechanical interaction is
typically realized using a mechanically compliant capacitance,
which transfers a mechanical displacement into a change of the
resonance frequency of the microwave circuit[10–14,17]. It was pro-
posed early on that inductive coupling schemes can allow for
higher coupling rates than capacitive ones[18–21].

SQUID tunable microwave resonators can be designed to
realize qubits or effective two-level systems[22,23]. In this context,
electromechanical interactions have also been studied[15,24–27]
enabling large optomechanical couplings with the potential to
realize quantum interference of massive objects' trajectories[28]. In
addition, they provide a route to implement even more complex
coupled quantum systems, which, e.g., allow to create
photon–phonon entanglement, phonon Fock state generation,
and three partite entanglement[29–31]. However, these systems
employ the effective two-level character and hence go beyond the
traditional optomechanical system.

Only recently, an electromechanical coupling on-par with
capacitive approaches was demonstrated by using an inductive
coupling scheme based on a lumped-element microwave reso-
nator and a mechanically compliant Josephson inductance[32]. By
design, the linear inductance of the resonator was chosen much
larger than the Josephson inductance, limiting the coupling
strength in favor of tolerating large photon numbers. Com-
plementary, it was shown that a distributed resonator with an
embedded Josephson inductance allows to design arbitrarily large
nonlinearities and can be used to realize two-level systems[33].

Here, we present such an inductive coupling scheme based on a
Josephson nonlinearity integrated into a coplanar waveguide
resonator (CPW). For this device, we find a magnetic field tun-
able electromechanical vacuum coupling of up to 1.62 kHz.

Moreover, we find a proportionality factor of 3.1 MHz T^{-1},
between the coupling rate and the applied magnetic field,
exceeding the one reported in ref. [32] by a factor of 120. In
addition, the high coupling rate allows us to detect the mechan-
ical motion with probe powers of 2.7 fW corresponding to an
occupation of the microwave resonator with only a few photons.
Hence, our device concept is naturally compatible with quantum
microwave sources, which typically offer only a limited output
power, and quantum-limited amplifiers with low saturation
powers. These benefits make the device class ideally suited to act
as a building block for the realization of inductively coupled
devices integrated in more complex quantum circuits. Our results
represent a significant step toward reaching the single-photon
strong-coupling regime in electromechanics, allowing the inves-
tigation of quantum mechanical effects such as single-photon
single-phonon blockade[4,34], the creation of mechanical quantum
states[35], and the generation of non-classical light[36].

Results and discussion
Circuit concept and fabrication. The nano-electromechanical
device discussed here is based on a $\lambda/4$ superconducting CPW
resonator which is shunted to ground at one of its ends via a
direct-current superconducting quantum interference device (dc-
SQUID) (cf. Fig. 1). As the SQUID acts as a flux-dependent
inductance, the resonance frequency of the microwave circuit
becomes flux sensitive. In addition, the SQUID loop is partly
suspended and contains two nanomechanical string oscillators.
Any displacement x of the strings translates into a change of the
magnetic flux Φ threading the SQUID loop and, in turn, into the
microwave resonance frequency ω_c. The mechanically induced
frequency shift can be described by the electromechanical inter-
action Hamiltonian $\hat{H}_{int} = \hbar g_0 \hat{a}^\dagger \hat{a}(\hat{b}^\dagger + \hat{b})$, where $\hat{a}$ ($\hat{b}$) are the
ladder operators of the microwave resonator (mechanical oscil-
lator). The electromechanical coupling constant[18,19,21,37]

$$g_0 = \frac{\partial \omega_c}{\partial \Phi} \delta\Phi = \frac{\partial \omega_c}{\partial \Phi} \gamma B_{ext} l x_{zpm}, \qquad (1)$$

scales with the length l of the string, the zero-point displacement
$x_{zpm} = \sqrt{\hbar/2m_{eff}\Omega_m}$, and the mode-shape γ of the mechanical
resonator. Note, that g_0 is tunable as the applied magnetic field
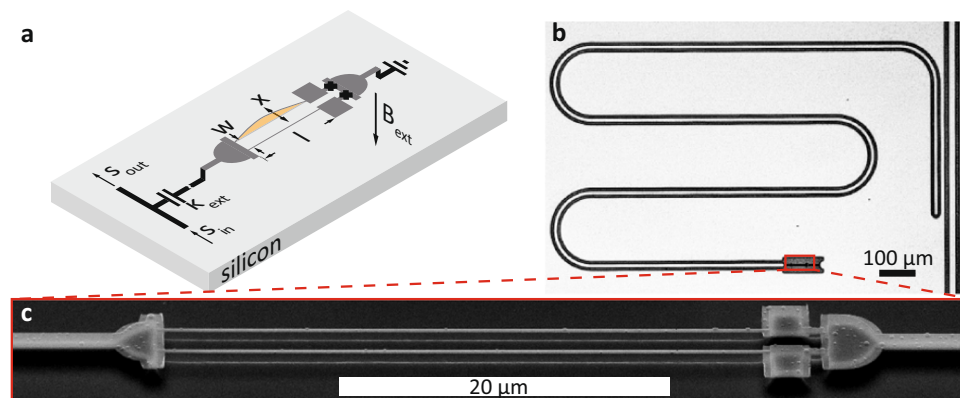
Fig. 1 Sample schematic and device images. Panel **a** shows a schematic of the device. The superconducting $\lambda/4$-coplanar microwave resonator is coupled
capacitively with a coupling rate κ_{ext} to a microwave transmission line acting as feed-line, where S_{in} and S_{out} denote the microwave input and output signal.
A dc-SQUID with two freely suspended arms, which are separated by w, shunts the resonator to ground on the other end. The resonance frequency is
tunable by varying the flux through the SQUID loop, e.g., by adjusting the external magnetic field B_{ext}. In addition, the freely suspended SQUID arms
(strings) modulate the SQUID inductance with the mechanical frequency via a change in the area of the SQUID loop and hereby realize the
electromechanical coupling. In total, we expect the presence of four mechanical modes (one in- and one out-of-plane for each of the two strings) in our
device. In our experiments, we focus only on one of them as sketched in panel (**a**). Panel **b** shows a microscope image of the aluminum resonator with the
SQUID located at one end fabricated using a lift-off process. Panel **c** shows a tilted scanning electron microscope (SEM) image of a similar partly
suspended SQUID structure. Note that the strings investigated in this work have dimensions of 20 μm × 110 nm × 200 nm.

Table 1 Summary of all sample parameters.

	Parameter	Value	Comments
String	Mechanical eigenfrequency	$\Omega_m/2\pi = 6.34316$ MHz	Mode 4
	Mechanical linewidth (FWHM)	$\Gamma_m/2\pi = 25$ Hz	$T = 110$ mK
	Length of the string	$l = 20$ μm	
	Cross-section of the string	$S = w \times t = 110 \times 200$ nm^2	
	Tensile stress of the string	$\sigma = 170$ MPa	$T = 110$ mK
	Young's modulus (aluminum)	$E_Y = 70$ GPa	[49]
CPW	Bare CPW eigenfrequency	$\omega_0/2\pi = 9.85$ GHz	
	CPW length	$l_c = 2.930$ mm	
	CPW dimensions (width, gap)	$w_c = 10$ μm, $s_c = 8$ μm	
	CPW resonator inductance, capacitance	$L_c = 1.17$ nH, $C_c = 224$ fF	
	CPW impedance	$Z = 56\,\Omega$	
	Eff. dielectric constant	$\epsilon_{eff} = 6.45$	
SQUID	SQUID inductances	$L_{kin} = 41$ pH, $L_{geo} = 19$ pH	
	Josephson inductance	$L_J = 0.36$ nH	At sweet spot
	Critical current	$I_c = 442$ nA	Single junction
	Loop area	$A_{loop} = 44.6$ μm^2	
	Screening parameter	$\beta_L = 0.013$	
FTR	Sweet spot frequency	$\omega_c/2\pi = 7.445$ GHz	
	Sweet spot intrinsic linewidth	$\kappa_{int}/2\pi = 2$ MHz	$T = 110$ mK
	External microwave coupling	$\kappa_{ext}/2\pi = 0.5$ MHz	

For clarity, we have structured the sample's characteristics in terms of the mechanical nanostring (String), the coplanar waveguide resonator (CPW), the employed superconducting quantum interference device (SQUID), and flux-tunable resonator (FTR).

B_{ext} and the flux to resonance frequency transfer function $\partial\omega_c/\partial\Phi$, which we call in the following flux responsivity, can be controlled in situ.

We fabricate the electromechanical system as an all-aluminum superconducting circuit using electron beam lithography, double-layer shadow evaporation, and reactive ion etching (cf. Fig. 1 and Supplementary Note 3 for details). The SQUID contains two freely suspended mechanical string oscillators as well as the two Josephson junctions. Each string has a length $l = 20$ μm, a width $w = 200$ nm, and a thickness $t = 110$ nm, corresponding to an effective mass of $m_{eff} = 0.6$ pg (all parameters of the device are summarized in Table 1). During the device fabrication, we anneal the entire chip at 350 °C resulting in tensile stressed aluminum strings with mechanical resonance frequencies $\Omega_m \simeq 6.3$ MHz at millikelvin temperatures. Thus, we obtain a zero-point fluctuation of $x_{zpm} = 47$ fm. The microwave resonator is coupled capacitively at one of its ends to a microwave CPW feed-line, enabling the microwave spectroscopy of the device. The other end, is shunted to ground via the SQUID. In this way, we obtain a flux-tunable resonator with large flux responsivity $\partial\omega_c/\partial\Phi$, which is essential for the realization of a large electromechanical coupling strength.

Microwave resonator characterization. We start the characterization of the microwave circuit by performing microwave transmission measurements as shown in Fig. 2 (see Supplementary Note 1 B for details). Figure 2a shows the data as a function of the applied flux Φ, where the resonator appears as an absorption signature in dark blue. Figure 2b, c shows transmission data for two selected flux bias. For a quantitative analysis of the evolution of the microwave resonance frequency ω_c, we locate the transmission minimum for each flux bias and plot ω_c as well as $\partial\omega_c/\partial\Phi$ versus the applied flux in Fig. 2d, e. We find that $\partial\omega_c/\partial\Phi$ reaches values of up to 10 GHz/Φ_0, underlining the performance of this coupling scheme. In addition, the $\omega_c(\Phi)$ dependence allows us to extract the single-junction critical current of the SQUID, $I_c = 0.44$ μA, and the minimum Josephson inductance, $L_J = 0.36$ nH, at $\partial\omega_c/\partial\Phi = 0$ (see Supplementary Note 2). Recording transmission data for selected flux bias points with higher frequency resolution (as shown in Fig. 2b, c) allows us to

determine the external coupling rate κ_{ext} between the resonator and the feed-line as well as the internal loss rate κ_{int} of the microwave circuit. At $\partial\omega_c/\partial\Phi = 0$, we find a total linewidth of $\kappa/2\pi = (\kappa_{int} + \kappa_{ext})/2\pi = 2.5$ MHz. Figure 2f shows κ_{ext} and κ_{int} as a function of the flux responsivity. While κ_{ext} remains nearly constant, κ_{int} increases for large $\partial\omega_c/\partial\Phi$, which is attributed to the increased sensitivity of the circuit to flux noise. However, even at the bias point K, the device remains in the resolved sideband regime ($\Omega_m > \kappa$).

Quantification of the electromechanical readout performance. Next, we investigate the mechanical properties including the electromechanical coupling rate. For this experiment, we probe the microwave sideband fluctuations originating from the interaction of the incident probe tone with the mechanics. The probe tone is set to a blue sideband configuration ($\omega_p = \omega_c + \Omega_m$) to enable a sensitive detection of the scattered photons[4]. The resulting signal is down-converted with ω_p. Figure 3a shows the voltage power spectral density $S_{UU}(\Omega)$ detected using a spectrum analyzer (cf. Supplementary Note 1) for a temperature of 185 mK, when the microwave resonator is biased to working point K at $\omega_c/2\pi = 6.887$ GHz with $B_{ext} = -470$ μT. We find a mechanical signature with a resonance frequency $\Omega_m/2\pi = 6.34311$ MHz and a full-width at half-maximum linewidth of $\Gamma_m/2\pi = 33.6$ Hz. In addition, we modulate the frequency of the incident microwave probe tone resulting in a calibration peak visible in panel a at ~ -2 kHz. Similar to refs. [12,38], the comparison of the calibration tone amplitude $S_{UU}(\Omega_{mod})$ with the mechanical response $S_{UU}(\Omega_m)\Gamma_m/2$ allows us to quantify the electromechanical coupling rate g_0. Due to the specific detection scheme used for this experiment, we need to account for an additional factor $\mathcal{Y}$, which relates the transfer function of the mechanical motion to the transmission function of the calibration tone (refer to Supplementary Note 4 for details). From this data, we obtain $g_0/2\pi = (1.62 \pm 0.12)$ kHz. This value exceeds the highest coupling rate of 280 Hz[17] achieved for capacitive coupling by a factor of 5.8 and corresponds to a single-photon cooperativity C_0 of about 0.1. This large coupling strength allows us to use ultra-low probe powers for the detection of the mechanical sidebands. In fact, we use a
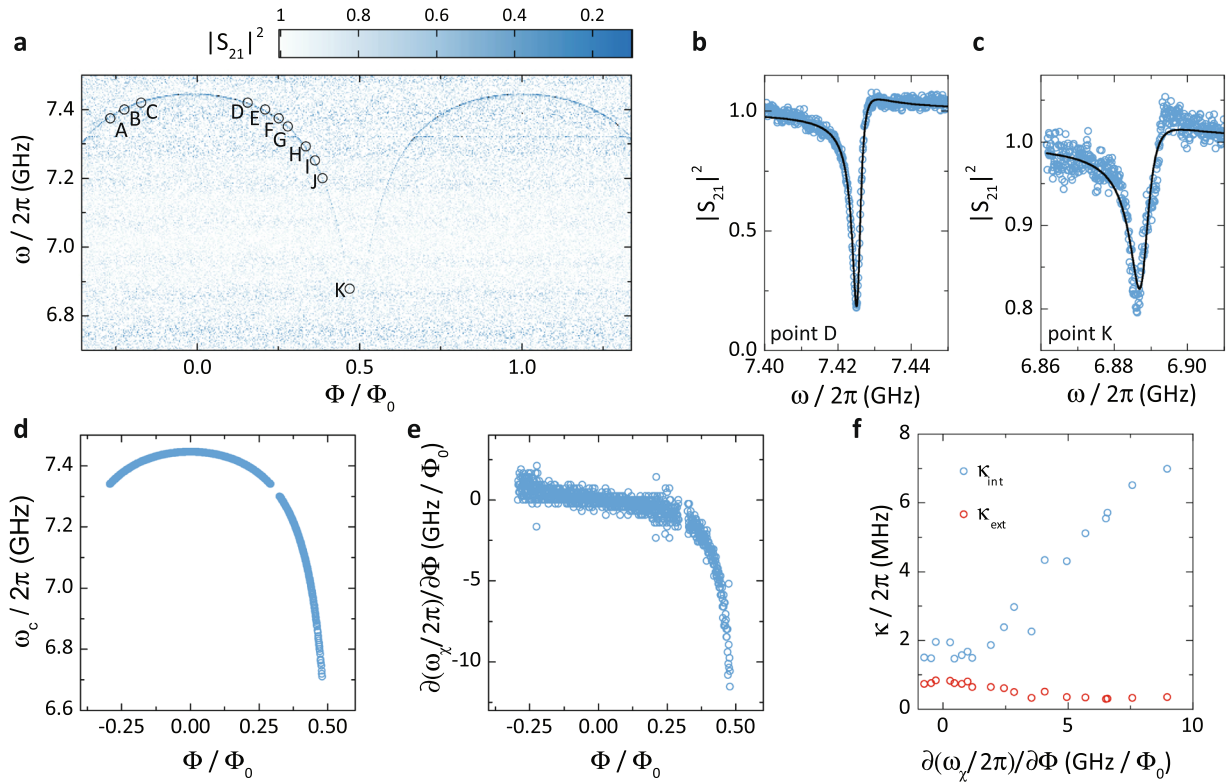
Fig. 2 Flux tuning of the microwave resonator. Panel **a** shows the calibrated microwave transmission as a function of the normalized applied magnetic flux. The tunable resonator exhibits a maximum frequency of 7.45 GHz and remains visible down to ≈6.7 GHz. Around 7.3 GHz, we find a parasitic resonance, which we avoid in our experiments. In addition, we perform a detailed analysis of the electromechanical coupling rate at the operation points indicated. Panels **b** and **c** display the transmission data at points D and K as well as a fit, which allows to quantify the internal and external loss rates of the microwave resonator. Panel **d** displays the evolution of the microwave resonance frequency as function of the flux bias. The flux to resonance frequency transfer function $\partial\omega_c/\partial\Phi$ is computed from this data and shown in panel (**e**), demonstrating responsivities exceeding 10 GHz/Φ_0. To judge whether the device operates in the resolved sideband regime, we analyse the transmission data for all operation points and extract the internal and external loss rates as depicted in panel (**f**). While the external coupling rate is rather constant, the internal loss rate increases with increasing responsivity $\partial\omega_c/\partial\Phi$.
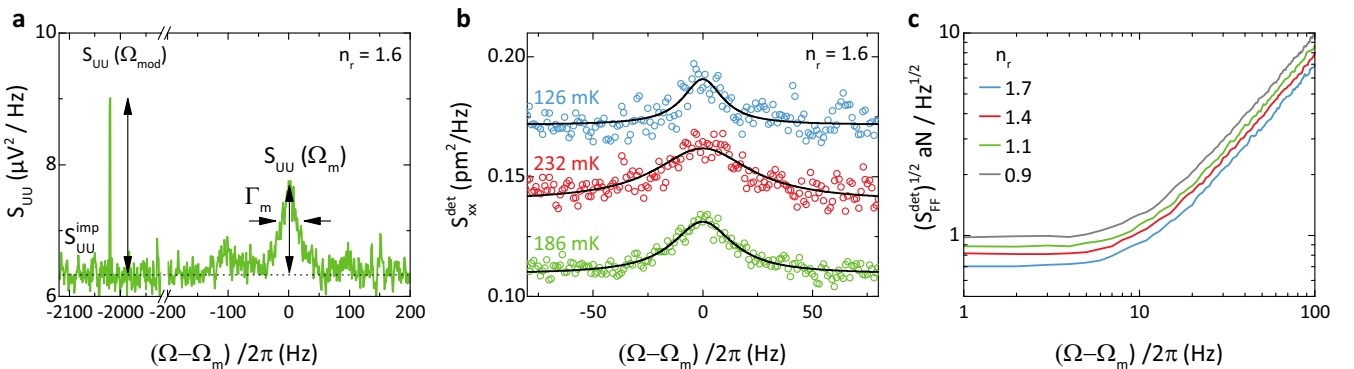
Fig. 3 Thermal mechanical displacement noise. Panel **a** shows the voltage noise spectral density S_{UU} of the down-converted microwave spectroscopy tone. At $\Omega_m/2\pi = 6.34311$ MHz, we observe the mechanical signature with a peak amplitude of $S_{UU}(\Omega_m) = 1.26$ μV^2 Hz^{-1} and a linewidth of $\Gamma_m/(2\pi) = 33.6$ Hz. In this experiment, we configure the microwave spectroscopy tone to the blue sideband configuration ($\omega_p = \omega_c + \Omega_m$) to efficiently detect the Stokes field within the bandwidth of the resonator. However, we suppress back-action induced heating by using an ultra-weak probe tone corresponding to an average photon number of $\bar{n}_r = 1.6$ in the microwave resonator. The sharp peak at $(\Omega - \Omega_m)/2\pi \approx -2$ kHz with an amplitude of $S_{UU}(\Omega_{mod}) = 2.56$ μV^2 Hz^{-1} stems from the phase modulation of the microwave spectroscopy tone ($\phi_0 = 3.94 \times 10^{-4}$). Combining the information of the mechanical signature and the calibration peak, we find an electromechanical vacuum coupling of $g_0/2\pi = (1.62 \pm 0.12)$ kHz. We further show the mechanical displacement density S_{xx}^{det} in panel (**b**) for $T = 126$ mK (blue), 186 mK (green), and 232 mK (red dots) including the Lorentzian fits to the data (solid lines). The peak area scales as expected with temperature via the mechanical linewidth. All spectra are recorded with the same averaging. Panel **c** shows the spectral force sensitivity S_{FF}^{det} at $T = 126$ mK for the microwave probe powers as indicated. On-resonance, we reach sub-attonewton force sensitivities even for these ultra-low microwave probe powers.

probe power corresponding to an average photon number of $\bar{n}_r = 1.6$ in the microwave resonator for the spectrum shown in Fig. 3a. At this power level, we suppress back-action induced heating of the mechanical mode. In particular, for the parameters used in our experiment, we estimate an electromechanically induced damping rate of $|\Gamma_{em} = -2.6\,\mathrm{Hz}| \ll \Gamma_m$, resulting in an increase in the thermal phonon occupation by 4%[4], as we probe with a cooperativity of $C \simeq C_0 \simeq 0.1$. This contribution is already accounted for in the stated value of g_0 (for details see Supplementary Note 5). The background of $S_{UU}(\Omega)$ shows the experimental imprecision noise S_{UU}^{imp} of the experiment, which is presently limited by the performance of the cryogenic microwave amplifier used as the first amplification stage.

Our calibration technique allows us to express $S_{UU}(\Omega)$ as the mechanical displacement spectrum $S_{xx}(\Omega)$ (see Supplementary Note 4). Figure 3b displays these spectra for various temperatures. We observe the expected increase in the phonon number with temperature in the form of an enlarged peak area. This manifests itself as an enhancement of the linewidth Γ_m with temperature (cf. Supplementary Information, Fig. S10a). This behavior has been observed for aluminum nano-strings and is attributed to the reduced dimensionality (1D) of the phonon mode[39]. In addition, we find a non-monotonic dependence of the imprecision noise floor on the environmental temperature. This behavior correlates with the temperature-dependent quality factor of the microwave resonator, which decreases above 185 mK. We speculate that this observation is connected to its population with thermal microwave photons, the presence of quasiparticles, and the motion of flux vortices (for details see Supplementary Note 4B).

The detected displacement power spectral density S_{xx}^{det} directly relates to the force sensitivity S_{FF}^{det} via $S_{FF}^{det} = 2S_{xx}(\Omega)/|\chi|^2$[40] with the mechanical susceptibility $\chi = [m_{eff}(\Omega^2 - \Omega_m^2 - i\Gamma_m\Omega)]^{-1}$ (cf. Supplementary Note 6). For $T = 126$ mK, we find an on-resonance force sensitivity of $(S_{FF}^{det})^{1/2} = 0.70\,\mathrm{aN\,Hz^{-1/2}}$ (0.98 aN Hz$^{-1/2}$) for a probe tone power of 5.3 fW (2.7 fW) corresponding to $\bar{n}_r = 1.7$ (0.86) photons. Here, the large electromechanical coupling rate (cf. Fig. 3c) allows to operate the device at much lower power compared to capacitive electromechanical devices having demonstrated 0.54 aN Hz$^{-1/2}$ at probe powers of 1 pW[40].

Tuning of the vacuum coupling strength. Next, we investigate the scaling of the electromechanical coupling strength with the applied magnetic field B_{ext} and the flux responsivity $\partial\omega_c/\partial\Phi$, cf. Eq. (1). To this end, we excite the mechanical motion using an oscillatory mechanical force provided by piezo actuators resulting in a controlled oscillating displacement of the nano-strings. Under these conditions, the displacement amplitude is much larger compared to the thermal noise-driven measurements and hence much easier to detect (details are found in Supplementary Note 7). Figure 4a shows the measured resonance frequency shift of the microwave resonator $\delta\omega_c$ for various flux responsivities using a coherent excitation force at an approximately constant magnetic field of $B_{ext} \approx -440\,\mu\mathrm{T}$. As the frequency shift $\delta\omega_c$ is proportional to the product $(\partial\omega_c/\partial\Phi)\delta\Phi$, we observe a large $\delta\omega_c$ for large flux responsivity $\partial\omega_c/\partial\Phi$. Figure 4b summarizes the coupling rates derived from the peak amplitudes presented in Fig. 4a (dark green triangles) as well as the results of further experiments with a lower piezo actuator drive power (light green triangles) and links them to displacement noise measurements of g_0 (red cross). The data corroborate the predicted linear scaling of the electromechanical coupling with the flux responsivity of up to 10 GHz/Φ_0.

In a similar fashion, we measure the electromechanical response as a function of the applied magnetic field for a fixed flux responsivity of $\partial(\omega_c/2\pi)/\partial\Phi = 6.6\,\mathrm{GHz}/\Phi_0$ (bias point K) and present the data in Fig. 4c. Again, we link these data points to the thermal displacement measurements (red circles) and corroborate the linear scaling with B_{ext}.

From Fig. 4c, we extract a scaling factor of $(3.13 \pm 0.20)\,\mathrm{MHz\,T^{-1}}$ for the electromechanical coupling with respect to the applied magnetic field B_{ext}. This value exceeds those of previous reports by two orders of magnitude[32] and represents an important figure of merit as it allows one to estimate g_0 at the given physical parameters of the device. For example, for the 70 nm thin aluminum film, we expect an in-plane critical field of 130 mT[41] which extrapolates to $g_0/2\pi = 410$ kHz. This coupling rate does not yet satisfy the single-photon strong coupling condition. However, improved microwave decoherence rates of up to 400 kHz as reported for superconducting quantum circuits[42] in combination with an optimized critical current I_c of the SQUID will allow to reach the strong-coupling regime (see Supplementary Note 9). Nevertheless, ground-state cooling for $\bar{n}_r = 1$ is expected to be within reach for this device using moderate fields of $B_{ext} = 20$ mT applied in parallel to the superconducting layer. Overall, we find an improvement of the vacuum coupling strength by a factor of 7 in comparison to previous inductive coupling schemes[32].

Finally, Eq. (1) includes a mode-shape factor γ. With our experimental parameters outlined so far, we find $\gamma = 0.99$, which is in good agreement with previous findings[16,32].

Besides electromechanically induced transparency (EMIT), which can be used to measure g_0 given quantitative knowledge of the photon number[12,32,43–45], one can utilize the signature of a modification of the microwave resonator absorption lineshape, using the strong binding condition $\delta\omega_c > \Omega_m$[46] to confirm g_0. Given our parameters (see Table 1), we use the second strategy. Here, a large amplitude coherent oscillation of the displacement is excited by a coherent mechanical drive causing the characteristic pattern of the microwave resonator absorption lineshape. When combined with the nonlinear response of the string-oscillator, we can quantify the displacement and hence g_0. Corresponding data (shown in Supplementary Information, Fig. S12) corroborates the coupling strengths determined via thermal displacement noise (data analysis is presented in Supplementary Note 8).

Conclusions. In summary, we present a device implementing an inductive electromechanical coupling scheme based on a superconducting coplanar waveguide resonator and a dc-SQUID operating in the resolved sideband regime. We demonstrate an electromechanical coupling rate of 1.62 kHz, exceeding values of capacitive coupling schemes by almost an order of magnitude. This high coupling rate enables an ultra-high force sensitivity of 0.70 aN Hz$^{-1/2}$ at an ultra-low microwave readout power of 5.4 fW, making this device a very promising low-power force sensor. In addition, the maximum electromechanical coupling of 1.62 kHz in combination with the investigated tuning of the electromechanical coupling indicates that this coupling strategy has the potential to reach the single-photon strong-coupling regime of electromechanics. Moreover, the tunability of the coupling provides the access to new features of electromechanical systems such as state amplification and readout techniques using the resonator as a parametric amplifier.

During the review process, we became aware of similar works by refs. [47,48].

Methods
Calibration of the electromechanical coupling via thermal motion. For the determination of the electromechanical coupling constant, we use a scheme similar to the calibration tone technique discussed by Gorodetsky et al. in ref. [38]. In particular, we use the microwave detection scheme where the frequency modulates the microwave source to generate the calibration tone. We down-convert the signal
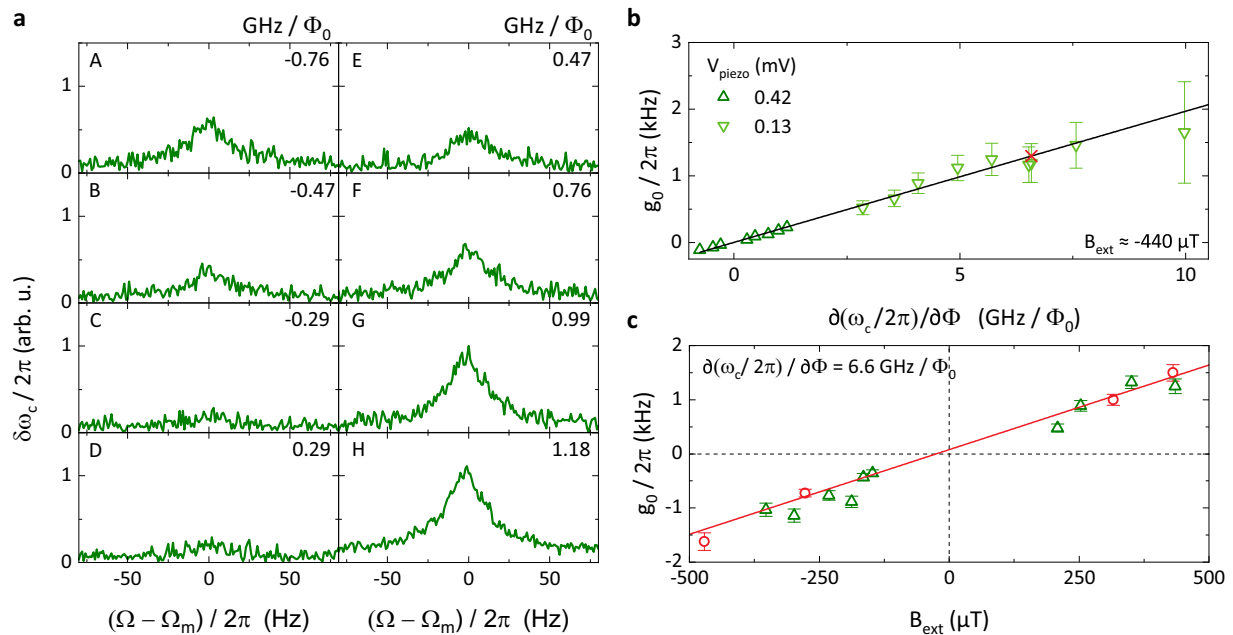
Fig. 4 Scaling of the electromechanical coupling rate at $T = 126$ mK. Panel **a** shows the mechanically driven resonator shift $\delta\omega_c$ close to Ω_m for a coherent mechanical drive at angular frequency Ω generated by a piezo actuator for the various operation points labeled in Fig. 2. The external static magnetic field is set to $B_{ext} \approx -440$ μT. At magnetic field bias points (e.g., C, D) with low flux responsivity, almost no mechanical signature is observed, in contrast to those points (E to H) with large flux responsivity. Panel **b** displays the electromechanical coupling rate g_0 deduced from the response in panel (**a**). The derived values are plotted versus the flux responsivity for low (light green triangles) and high piezo drive amplitudes (dark green triangles), and are linked to the thermal displacement measurements (red cross). This data confirms the linear scaling of the electromechanical coupling strength with $\partial\omega_c/\partial\Phi$. In panel **c**, we plot the coupling rate g_0 obtained both from driven (green) and thermal displacement measurements (red) versus the applied magnetic field B_{ext} for a fixed flux responsivity of $\partial(\omega_c/2\pi)/\partial\Phi = 6.6$ GHz/Φ_0. In the given experimental configuration, the external field sets the working point of the microwave resonator. As flux jumps occurred during the experiments the recorded driven measurements could not be performed at identical field bias as the thermal ones. The error bars on the data in panels (**b**) and (**c**) include the standard error originating from the model-fit to the data and errors originating from the calibration. If not shown, error bars are smaller than the symbol size.

coming from the dilution fridge with an unmodulated local oscillator and perform a spectrum analysis of the down-converted signal. This results in the spectra shown in Fig. 3a. Via this scheme, the vacuum coupling strength is determined by

$$g_0^2 = \frac{1}{2n_m}\frac{\Omega_m^2 \phi_0^2}{2}\frac{\Gamma_m}{4}\frac{1}{\mathcal{Y}}\frac{1}{\text{ENBW}}\frac{S_{UU}(\Omega_m)}{S_{UU}(\Omega_{mod})}. \qquad (2)$$

This is derived in full detail in Supplementary Note 4

Determination of the resonator transfer function. For a quantitative analysis of Eq. (2), we need to obtain information about the transfer functions $\mathcal{Y}$ involved as well. For our case, we find the transfer function depending in general on the microwave resonator characteristics and the employed probe tone configuration

$$\mathcal{Y} \approx \frac{16\eta^2\kappa^2\Omega_m^2}{(4\Delta^2 + \kappa^2)\big(4(\Delta - \Omega_m)^2 + (1 - 2\eta)^2\kappa^2\big)}, \qquad (3)$$

as we derive in more detail in Supplementary Note 4A.

Scaling of the electromechanical coupling. Due to the nature of the inductive coupling, the electromechanical coupling rate is flux tunable (see Eq. (1)). Thus, we expect a linear scaling of the electromechanical coupling rate with $\partial\omega_c/\partial\Phi$ and B_{ext}. As discussed in the main text, one option to explore the scaling of g_0 are thermal displacement noise experiments. Alternatively, and more time efficiently, one can measure the frequency shift of the microwave resonator for a fixed mechanical excitation amplitude. In this experiment, the signal amplitudes are significantly larger resulting in a faster data acquisition. In detail, we use a piezo actuator mounted on the outside of the sample enclosure to excite the nanostring. The piezo actuator is addressed using a fixed excitation voltage. As the displacement strength is independent of $\partial\omega_c/\partial\Phi$ and B_{ext}, the piezo actuator induces a displacement of constant amplitude. Thus, the recorded frequency shift $\delta\omega_c$ is determined only by the coupling strength, without the need for a calibration of the piezo susceptibility. If a quantification of the vacuum coupling strength is desired, the extracted frequency shift has to be calibrated independently. For that purpose, we use the spectroscopy of the nanostring's thermal motion.

Data availability

Experimental data are available upon reasonable request at the corresponding author.

References

1. Leggett, A. J. Testing the limits of quantum mechanics: motivation, state of play, prospects. *J. Phys. Condens. Matter.* **14**, 415 (2002).
2. Poot, M. & van der Zant, H. S. J. Mechanical systems in the quantum regime. *Phys. Rep.* **511**, 273 (2012).
3. Ockeloen-Korppi, C. F. et al. Noiseless quantum measurement and squeezing of microwave fields utilizing mechanical vibrations. *Phys. Rev. Lett.* **118**, 103601 (2017).
4. Aspelmeyer, M., Kippenberg, T. J. & Marquardt, F. Cavity optomechanics. *Rev. Mod. Phys.* **86**, 1391 (2014).
5. Abbott, B. P. et al. Observation of gravitational waves from a binary black hole merger. *Phys. Rev. Lett.* **116**, 061102 (2016).
6. Moser, J. et al. Ultrasensitive force detection with a nanotube mechanical resonator. *Nat. Nanotechnol.* **8**, 493 (2013).
7. Wollman, E. E. et al. Quantum squeezing of motion in a mechanical resonator. *Science* **349**, 952 (2015).
8. Lei, C. U. et al. Quantum nondemolition measurement of a quantum squeezed state beyond the 3 db limit. *Phys. Rev. Lett.* **117**, 100801 (2016).
9. Aspelmeyer, M., Meystre, P. & Schwab, K. Quantum optomechanics. *Phys. Today* **65**, 29 (2012).
10. Regal, C. A., Teufel, J. D. & Lehnert, K. W. Measuring nanomechanical motion with a microwave cavity interferometer. *Nat. Phys.* **4**, 555 (2008).
11. Teufel, J. D. et al. Sideband cooling of micromechanical motion to the quantum ground state. *Nature* **475**, 359 (2011).
12. Zhou, X. et al. Slowing, advancing and switching of microwave signals using circuit nanoelectromechanics. *Nat. Phys.* **9**, 179 (2013).

13. Weber, P., Güttinger, J., Tsioutsios, I., Chang, D. E. & Bachtold, A. Coupling graphene mechanical resonators to superconducting microwave cavities. *Nano Lett.* **14**, 2854 (2014).

14. Singh, V. et al. Optomechanical coupling between a multilayer graphene mechanical resonator and a superconducting microwave cavity. *Nat. Nanotechnol.* **9**, 820 (2014).

15. Pirkkalainen, J.-M. et al. Cavity optomechanics mediated by a quantum two-level system. *Nat. Commun.* **6**, 6981 (2015).

16. Etaki, S. et al. Motion detection of a micromechanical resonator embedded in a d.c. SQUID. *Nat. Phys.* **4**, 785 (2008).

17. Reed, A. P. et al. Faithful conversion of propagating quantum information to mechanical motion. *Nat. Phys.* **13**, 1163 (2017).

18. Blencowe, M. P. & Buks, E. Quantum analysis of a linear dc SQUID mechanical displacement detector. *Phys. Rev. B* **76**, 014511 (2007).

19. Nation, P., Blencowe, M. & Buks, E. Quantum analysis of a nonlinear microwave cavity-embedded dc SQUID displacement detector. *Phys. Rev. B* **78**, 104516 (2008).

20. Nation, P. D., Suh, J. & Blencowe, M. P. Ultrastrong optomechanics incorporating the dynamical Casimir effect. *Phys. Rev. A* **93**, 022510 (2016).

21. Shevchuk, O., Steele, G. A. & Blanter, Y. M. Strong and tunable couplings in flux-mediated optomechanics. *Phys. Rev. B* **96**, 014508 (2017).

22. Wallraff, A. et al. Strong coupling of a single photon to a superconducting qubit using circuit quantum electrodynamics. *Nature* **431**, 162 (2004).

23. Koch, J. et al. Charge-insensitive qubit design derived from the cooper pair box. *Phys. Rev. A* **76**, 042319 (2007).

24. Pirkkalainen, J.-M. et al. Hybrid circuit cavity quantum electrodynamics with a micromechanical resonator. *Nature* **494**, 211 (2013).

25. Viennot, J. J., Ma, X. & Lehnert, K. W. Phonon-number-sensitive electromechanics. *Phys. Rev. Lett.* **121**, 183601 (2018).

26. Sletten, L. R., Moores, B. A., Viennot, J. J. & Lehnert, K. W. Resolving phonon Fock states in a multimode cavity with a double-slit qubit. *Phys. Rev. X* **9**, 021056 (2019).

27. Moores, B. A., Sletten, L. R., Viennot, J. J. & Lehnert, K. W. Cavity quantum acoustic device in the multimode strong coupling regime. *Phys. Rev. Lett.* **120**, 227701 (2018).

28. Khosla, K. E., Vanner, M. R., Ares, N. & Laird, E. A. Displacemon electromechanics: how to detect quantum interference in a nanomechanical resonator. *Phys. Rev. X* **8**, 021052 (2018).

29. Abdi, M., Pernpeintner, M., Gross, R., Huebl, H. & Hartmann, M. J. Quantum state engineering with circuit electromechanical three-body interactions. *Phys. Rev. Lett.* **114**, 173602 (2015).

30. Kounalakis, M., Blanter, Y. M. & Steele, G. A. Synthesizing multi-phonon quantum superposition states using flux-mediated three-body interactions with superconducting qubits. *NPJ Quant. Inf.* **5**, 100 (2019).

31. Wang, Y.-D., Chesi, S. & Clerk, A. A. Bipartite and tripartite output entanglement in three-mode optomechanical systems. *Phys. Rev. A* **91**, 013807 (2015).

32. Rodrigues, I. C., Bothner, D. & Steele, G. A. Coupling microwave photons to a mechanical resonator using quantum interference. *Nat. Commun.* **10**, 5359 (2019).

33. Bourassa, J., Beaudoin, F., Gambetta, J. M. & Blais, A. Josephson-junction-embedded transmission-line resonators: from Kerr medium to in-line transmon. *Phys. Rev. A* **86**, 013814 (2012).

34. Nunnenkamp, A., Borkje, K. & Girvin, S. Single-photon optomechanics. *Phys. Rev. Lett.* **107**, 063602 (2011).

35. Lü, X.-Y. et al. Squeezed optomechanics with phase-matched amplification and dissipation. *Phys. Rev. Lett.* **114**, 093602 (2015).

36. Qian, J., Clerk, A., Hammerer, K. & Marquardt, F. Quantum signatures of the optomechanical instability. *Phys. Rev. Lett.* **109**, 253601 (2012).

37. Buks, E., Zaitsev, E., Segev, E., Abdo, B. & Blencowe, M. Displacement detection with a vibrating rf superconducting interference device: beating the standard linear limit. *Phys. Rev. E* **76**, 026217 (2007).

38. Gorodetsky, M. L., Schliesser, A., Anetsberger, G., Deleglise, S. & Kippenberg, T. J. Determination of the vacuum optomechanical coupling rate using frequency noise calibration. *Opt. Express* **18**, 23236 (2010).

39. Hoehne, F. et al. Damping in high-frequency metallic nanomechanical resonators. *Phys. Rev. B* **81**, 231 (2010).

40. Teufel, J. D., Donner, T., Castellanos-Beltran, M. A., Harlow, J. W. & Lehnert, K. W. Nanomechanical motion measured with an imprecision below that at the standard quantum limit. *Nat. Nanotechnol.* **4**, 820 (2009).

41. Meservey, R. & Tedrow, P. M. Properties of very thin aluminum films. *J. Appl. Phys.* **42**, 51 (1971).

42. Schneider, A. et al. Transmon qubit in a magnetic field: evolution of coherence and transition frequency. *Phys. Rev. Res* **1**, 023003 (2019).

43. Weis, S. et al. Optomechanical induced transparency. *Science* **330**, 1520 (2010).

44. Hocke, F. et al. Electromechanically induced absorption in a circuit nano-electromechanical system. *New J. Phys.* **14**, 123037 (2012).

45. Yuan, M., Singh, V., Blanter, Y. M. & Steele, G. A. Large cooperativity and microkelvin cooling with a three-dimensional optomechanical cavity. *Nat. Commun.* **6**, 8491 (2015).

46. Schliesser, A., Rivière, R., Anetsberger, G., Arcizet, O. & Kippenberg, T. J. Resolved-sideband cooling of a micromechanical oscillator. *Nat. Phys.* **4**, 415 (2008).

47. Zoepfl, D., Juan, M. L., Schneider, C. M. F. & Kirchmair, G. Single-photon cooling in microwave magnetomechanics. *Phys. Rev. Lett.* **125**, 023601 (2020).

48. Bera, T., Majunder, S., Kumar, S. & Singh, V. Large flux-mediated coupling in hybrid electromechanical system with a transmon qubit. Preprint at https://arxiv.org/pdf/2001.05700.pdf (2020).

49. Sulkko, J. et al. Strong gate coupling of high-Q nanomechanical resonators. *Nano Lett.* **10**, 4884 (2010).

Author contributions

M.A. and P.S. designed and fabricated the sample. P.S. performed the experiments. H.H. and P.S. build the measurement setup. S.P., P.S., and H.H. performed theoretical modeling and analysis of the data. H.H., P.S., and R.G. wrote the paper. H.H. and R.G. conceived the experiment. F.D. and A.M. supported the SQUID fabrication. H.H., R.G., F.D., and A.M. supervised the project. All authors discussed the results and contributed to the manuscript.

Competing interests

The authors declare no competing interests.

Additional information

Supplementary information is available for this paper at https://doi.org/10.1038/s42005-020-00501-3.

Correspondence and requests for materials should be addressed to H.H.

Reprints and permission information is available at http://www.nature.com/reprints

Publisher's note Springer Nature remains neutral with regard to jurisdictional claims in published maps and institutional affiliations.